LAWRENCE
LIVERMORE
NATIONAL
LABORATORY

LLNL-TR-660055

SIMS Analyses of Aerodynamic Fallout from a Uranium-Fueled Test

L. A. Lewis, K. B. Knight, J. E. Matzel, S. G. Prussin, F. J. Ryerson, W. Kinman, M. M. Zimmer, I. D. Hutcheon

September 9, 2014

Disclaimer

This document was prepared as an account of work sponsored by an agency of the United States government. Neither the United States government nor Lawrence Livermore National Security, LLC, nor any of their employees makes any warranty, expressed or implied, or assumes any legal liability or responsibility for the accuracy, completeness, or usefulness of any information, apparatus, product, or process disclosed, or represents that its use would not infringe privately owned rights. Reference herein to any specific commercial product, process, or service by trade name, trademark, manufacturer, or otherwise does not necessarily constitute or imply its endorsement, recommendation, or favoring by the United States government or Lawrence Livermore National Security, LLC. The views and opinions of authors expressed herein do not necessarily state or reflect those of the United States government or Lawrence Livermore National Security, LLC, and shall not be used for advertising or product endorsement purposes.

This work performed under the auspices of the U.S. Department of Energy by Lawrence Livermore National Laboratory under Contract DE-AC52-07NA27344.

Spatially-Resolved Analyses of Aerodynamic Fallout from a Uranium-Fueled Nuclear Test

L.A. Lewis[a,b,1], K.B. Knight[a], J.E. Matzel[a], S.G. Prussin[c], M.M. Zimmer[c], W.S. Kinman[c], F.J. Ryerson[a] and I.D. Hutcheon[a]

[a] Glenn Seaborg Institute, *Lawrence Livermore National Laboratory, 7000 East Avenue, Livermore, CA 94550, USA*
[b] Dept. of Nuclear Engineering, *University of California, Berkeley, 4113 Etcheverry Hall MC 1730, Berkeley, CA 94720, USA*
[c] Nuclear and Radiochemistry Group, *Los Alamos National Laboratory*, *Bikini Atoll Rd. SM 30, Los Alamos, NM 87545, USA*

Highlights

- Spatially-resolved measurements of unfissioned fuel in fallout elucidates fallout formation processes
- Our data capture both striking homogeneity and heterogeneity in the distribution of unfissioned fuel in fallout
- These distributions reflect formation processes that including heating to high temperatures, molten agglomeration of heterogeneous and possibly homogenous precursors, variable degrees of physical mixing, and rapid cooling

Keywords: SIMS; trinitite; fallout; device debris; nuclear forensics

Abstract

Five silicate fallout glass spherules produced in a uranium-fueled, near-surface nuclear test were characterized by secondary ion mass spectrometry, electron probe microanalysis, autoradiography, scanning electron microscopy, and energy-dispersive x-ray spectroscopy. Several samples display distinctive compositional heterogeneity suggestive of incomplete mixing, and exhibit heterogeneity in U isotopes with $0.02 < {}^{235}U/{}^{238}U < 11.8$ among all five samples and $0.02 < {}^{235}U/{}^{238}U < 7.81$ within a single sample. In two samples, the ${}^{235}U/{}^{238}U$ ratio is correlated with major element composition, consistent with the agglomeration of chemically and isotopically distinct molten precursors. Two samples are quasi-homogeneous with respect to composition and uranium isotopic composition, suggesting extensive mixing possibly due longer residence time in the fireball. Correlated variations between ${}^{234}U$, ${}^{235}U$, ${}^{236}U$ and ${}^{238}U$ abundances point to mixing of end-members corresponding to uranium derived from the device and natural U (${}^{238}U/{}^{235}U = 0.00725$) found in soil.

1. Introduction

There has been renewed interest in post-detonation fallout from surface or near-surface nuclear events (Parekh et al., 2006; Eby et al., 2010; Fahey et al., 2010; Belloni et al., 2011; Bellucci et al., 2012; Cassata et al., 2014; Eppich et al., 2014). During the era of above ground nuclear testing (1945-1973), the availability of quantitative microanalytical techniques for analysis of fallout was limited. The main focus of fallout analyses was to understand device performance and radiation effects, and spatially resolved analyses were generally limited to methods such as autoradiography to image the distribution of fission and activation products (Adams et al., 1960). Today, using modern microanalytical techniques, analyses of fallout can inform post-detonation nuclear forensic sample collection protocols and lead to a more

[1] Corresponding author. Tel.: +1 925-422-5377
E-mail address: lewis105@llnl.gov (Laurence Lewis).

comprehensive understanding of fallout formation, including improved constraints on formation mechanisms, timescales, and temperatures (Cassata et al., 2014; Eppich et al., 2014).

Glassy fallout forms when a nuclear device is detonated on or near the Earth's surface. Soil is melted and vaporized and swept into the fireball where it interacts with device components, fission and activation products, and unfissioned fuel (collectively 'device debris'; Brode, 1968; Glasstone and Dolan, 1977). Once the fireball cools below the condensation temperatures of elements in the debris cloud, particulates begin to condense and mix with upswept materials, isolating device debris within a matrix whose major element composition is largely reflective of the local geology and/or emplacement environment (Adams and O'Connor, 1957; Miller, 1964). The cooling timescale depends on device yield, but is estimated (Glasstone et al., 1977; Izrael, 2002) and measured to be on the order of seconds (Cassata et al., 2014). As fallout leaves the fireball, aerodynamic forces create a variety of distinctive shapes, often producing nearly-spherical objects (Crocker et al., 1965; Tompkins et al., 1970; Figure 1). Few studies have focused specifically on aerodynamic fallout glasses, but these objects are of particular interest due to their elevated concentrations of residual fuel and fission and activation products (Gostic et al., 2012; Eppich et al., 2014). Spatially-resolved analyses within individual samples may help elucidate sample formation mechanisms by revealing the distribution of residual fuel and potential correlations with major elements, distance from the center of a spherule, or other features.

Trinitite, the major component of fallout from the Trinity test, has been extensively studied over the past decade (Parekh et al., 2006; Eby et al., 2010; Fahey et al., 2010; Belloni et al., 2011; Bellucci et al., 2012; Bellucci et al., 2013; Wallace et al., 2013; Bellucci et al., 2014). These studies demonstrate that trinitite is compositionally heterogeneous due to incomplete mixing of partially melted and relic minerals found in the local geology, and it retains a heterogeneous distribution of fission products, device components, and unfissioned fuel. These observations in trinitite have yet to be compared with observations of aerodynamic fallout from Trinity or other nuclear tests.

In this study, we characterize the distribution of unfissioned fuel within aerodynamic glassy fallout from a uranium-fueled test using secondary ion mass spectrometry (SIMS) combined with scanning electron microscopy/energy-dispersive x-ray spectroscopy (SEM/EDS), electron microprobe microanalysis (EPMA), and autoradiography. For each sample we measured the extent of uranium isotopic heterogeneity, major element composition, and radioactivity and correlated these observations with spatial locations within individual spherules. We use these data to develop a simple model of fallout formation and present a two-component mixing model incorporating natural uranium from soil and/or the device and anthropogenic uranium from the device.

2. Materials and methods

2.1 Aerodynamic fallout samples

Five, millimeter-size aerodynamic fallout glasses were selected from soil collected from a uranium-fueled, near-surface nuclear test. The soil samples were collected about 120 meters from ground zero (along the path of the fallout plume). Glassy aerodynamic fallout is easily identifiable in soil collections (Figure 1) due to its smooth surface morphology and aerodynamic shape. The samples were isolated from the soils by visual inspection under an optical microscope, then weighed and photographed. Each piece of glass was mounted in epoxy and polished to expose an interior surface close to the mid-plane. Samples were coated with ~20 nm of carbon and characterized by autoradiography, SEM/EDS, EPMA, and SIMS (Figure 2).

[Figure 1]

The selected aerodynamic fallout samples range from 1.3-2.4 mm in diameter and 2.5-14.5 mg in mass (see Figure 2 for sample labels). They appear light grey to dark green or brown in color, and are optically translucent and glossy. Voids and bubbles are often visible within the volume of the glasses.

2.2 Experimental methods

2.2.1 SEM, EDS, and EPMA

Backscattered electron images of the samples were taken using an FEI Inspect-F SEM equipped with an AMETEK EDAX Apollo XL Si drift energy-dispersive x-ray spectrometer. The SEM was operated at an accelerating voltage of 20 kV with a beam current of ~1.5 nA.

Elemental maps and major element compositions were determined with a JEOL JXA-8200 electron microprobe equipped with 5 wavelength-dispersive spectrometers, and a JEOL energy-dispersive x-ray spectrometer. X-ray intensities were converted to concentrations using CITZAF (Armstrong, 1995). Operating conditions were 15 kV accelerating potential, 5 nA probe current and 2 μm beam diameter. The following silicate and oxide standards were used: orthoclase (Si, Al, K), Fe_2O_3 (Fe), spessartine (Mn), rutile (Ti), diopside (Ca), albite (Na), and MgO (Mg).The samples were analyzed for major element composition in rectangular arrays with 30 – 100 analyses per sample. Regions adjacent to vesicles and/or cracks and pits and that resulted in summed concentration totals of less than 98 wt% or greater than 102 wt% were excluded.

2.2.2 Sample autoradiography

To obtain autoradiographs, the samples were placed onto a photo-phosphor imaging plate for 34 hours inside a light-blocking tent. All 5 samples were exposed for the same length of time on a single plate at the same time. The plate was developed and then digitally read using a GE Typhoon 7000 scanner at a spatial resolution of ~50 μm/pixel. The autoradiographs record the distributions of β^- activity and near-surface α activity (respective mean free paths of ~1 cm and ~10 μm in silicates). For these five samples, the isotopes of uranium are the only anthropogenic α-emitting nuclides, and all have low specific activity. Therefore, the autoradiographs are dominated by the β^- activity in the samples. The long-lived fission products ^{137}Cs and ^{90}Sr are the dominant sources of β^- radioactivity in old samples and are likely to be major contributors to the β^- activity in these samples. In addition, the decay of the activation products ^{152,154}Eu has been measured in similar fallout samples (Gostic et al, 2012).

2.2.3 Spatially-resolved U isotope measurements

Spatially-resolved U isotope ratios were determined by secondary ion mass spectrometry (SIMS) in two separate analytical sessions, one at Lawrence Livermore National Laboratory (LLNL) using a modified Cameca ims-3f SIMS instrument to analyze four of the five glasses (U1A was not analyzed), and one at Los Alamos National Laboratory (LANL) using a Cameca ims-1280 SIMS to analyze all five glasses. No effort was made to reanalyze specific areas in the same samples. Approximately 20 spot analyses were performed per sample at LLNL and between 3 and 45 spot analyses were performed per sample at LANL (Figure 2).

The LLNL analyses were conducted using a 5 nA, $^{16}O^-$ primary ion beam that impacts the sample with a kinetic energy of 17 keV focused into a spot of ~10-30 μm diameter. Positive secondary ions were accelerated to 4500 V and passed through the mass spectrometer set to a mass resolving power of ~3000, sufficient to resolve most relevant molecular interferences. Data were collected using two different mass sequences. Initially, data were obtained for masses 250.8 (background), $^{235}U^{16}O$ and $^{238}U^{16}O$; the intensities of $^{234}U^{16}O$ and $^{236}U^{16}O$ were too low to measure with useful precision. In a second series of analyses, the mass table was expanded to include mass 29.8 (background) and mass 30 (^{30}Si) such that the U concentration at each analysis spot could be determined by comparing the $(^{235}U^{16}O^+ + ^{238}U^{16}O^+)/^{30}Si^+$ ratio to the same ratio measured in an aluminosilicate glass standard.

The analyses at LANL used a focused $^{16}O^-$ beam of 20-30 nA with a kinetic energy of 20 keV. Positive secondary ions were accelerated to 10 kV and detected using either mono-collection (magnetic peak switching with a single electron multiplier detector) or multi-collection (static magnetic field with multiple electron multiplier detectors). The ion transfer optics were tuned to image an 80 µm field of view using a 400 µm diameter contrast aperture and a 3000-4000 µm diameter field aperture. A mass resolving power of ~3000-4000 was used for both the mono-collector and the multi-collector analyses. Nuclear magnetic resonance control was used to stabilize the magnet for analyses performed by static multi-collection. A 40 x 40 µm area was pre-sputtered for 60 seconds, after which secondary ions were collected from a 25 x 25 µm rastered area for the mass sequence 233.8, ^{234}U, ^{235}U, ^{236}U and ^{238}U.

The accuracy and reproducibility of the SIMS U isotope analyses and instrumental mass bias for measurements made at LLNL and LANL were determined using a synthetic silicate glass doped with ~500 µg/g and ~5000 µg/g of U, respectively. Both glasses were doped with U having an isotope composition roughly equivalent to the U500 NIST standard. Using inductively-coupled plasma mass spectrometry (ICP-MS), the U isotope ratios in the ~500 µg/g glass (used at LLNL) were measured to be $^{235}U/^{238}U = 0.9618 \pm 0.0006$, $^{234}U/^{238}U = 0.010044 \pm 0.000015$, and $^{236}U/^{238}U = 0.001479 \pm 0.000007$. The U isotope ratios in the ~5000 µg/g glass (used at LANL) were measured to be $^{235}U/^{238}U = 0.9949 \pm 0.0014$, $^{234}U/^{238}U = 0.010371 \pm 0.000016$, and $^{236}U/^{238}U = 0.001521 \pm 0.000006$. The analyses at LLNL measured only ^{235}U and ^{238}U, while the LANL analyses measured four isotopes of U (^{234}U, ^{235}U, ^{236}U, and ^{238}U). The analyses of the standard at LLNL established a reproducibility (2σ) and accuracy of 0.2% in $^{235}U/^{238}U$. The reproducibility and accuracy of the LANL analyses are 0.09%, 0.02% and 0.7% for the $^{234}U/^{238}U$, $^{235}U/^{238}U$ and $^{236}U/^{238}U$ ratios, respectively, in mono-collection mode, and 0.2%, 0.04% and 0.7% for the same three ratios with multi-collection.

[Figure 2]

3. Results

3.1 Backscattered electron images and autoradiography

The backscattered electron images show that samples U1A and U1B are nearly spheroidal and nearly compositionally homogeneous (Figure 2). The polished section of U1A contains several large (10-100s of µm) spherical vesicles, while U1B has a nearly void-free interior. The regions appearing dark in the backscattered electron images in U1A and U1B are amorphous, nearly pure SiO_2. Sample U2 has an elongated, tear-drop shape with one large vesicle and multiple smaller vesicles, and exhibits much greater compositional heterogeneity than the four other samples; two major compositional zones are apparent in Figure 2. U3 is ~2.4 mm in maximum diameter and quasi-spherical with many vesicles clustered near the center. U3 exhibits some compositional heterogeneity (primarily in Si and Ca) on a spatial scale of tens of microns. U3 also contains several high Si regions that have sharply delineated boundaries. U4 is ~2.3 mm in maximum diameter and quasi-spherical, with no significant voids. The backscattered electron image of U4 shows well-defined compositional zones, many of which are approximately circular or ellipsoidal in cross section.

There are large differences in activity between the five samples, with U1A exhibiting much lower activity relative to U1B, which exhibits the highest activity (Figure 3). In U1A and U1B, activity is homogenously distributed, while U2, U3, and U4 display heterogeneous activity distributions. In U2, the areas with lowest activity correlate with the areas of lower average atomic number (lower brightness in the corresponding backscattered electron micrograph). However, U4 exhibits the opposite correlation: areas with lowest activity correlate with areas of higher average atomic number (higher brightness in the corresponding backscattered electron micrograph).

[Figure 3]

3.2 Major element compositions and element maps

Nine oxides account for ~99% of the composition of the glassy samples, as expected for materials primarily derived from the local soil exposed to an oxidizing environment. The results of the EMPA analyses (Table 1) indicate that all five samples have similar major element chemical compositions, enriched in Si (~72% SiO_2) and Al (~14% Al_2O_3). Two samples, U2 and U4, have regions characterized by two distinct compositions, indicated by the bright and dark regions in the respective backscattered electron images (Figure 2, Table 2). The relative standard deviation (the variation in the concentration compared to the average value) of the CaO content illustrates this difference: 7.5% for U1A versus 55% for U2 and 30% for U4. For U2, the CaO, Fe_2O_3, K_2O, and MgO concentrations are significantly different (>2σ) between the bright and dark regions in the backscattered electron image (the bright region is enriched in CaO, Fe_2O_3, and MgO and depleted in K_2O relative to the dark region). For U4, significant compositional differences occur for CaO, Al_2O_3, and SiO_2 (the bright region is enriched in CaO and Al_2O_3 and depleted in SiO_2 relative to the dark region).

[Table 1]

[Table 2]

[Figure 4]

3.3 Uranium isotope distributions

The variation in the $^{235}U/^{238}U$ isotope ratio spans a factor of nearly 600, from 0.02 to 11.8, across the five samples (Table 3; Figure 5). Within a single sample, U2, the $^{235}U/^{238}U$ ratio ranges from 0.02 to 7.8, a factor of nearly 400 (Figure 5). Similar variation was observed, but to a lesser degree, in ICP-MS analyses of whole spherules (Eppich et al., 2014) but has never before been observed within individual fallout samples. The minor isotope ratios, $^{234}U/^{238}U$ and $^{236}U/^{238}U$, also span a large range, a factor of over 200 (Figures 6 and 7; Table 3). On a 3-isotope plot, the minor U isotope ratios show a strong linear correlation among all five samples (Figures 6 and 7). For $^{234}U/^{238}U$ vs. $^{235}U/^{238}U$, a linear fit has $R^2 = 0.999$ and a slope of 0.010813 ± 0.000040 (2σ) and a y-intercept passing through the origin. For $^{236}U/^{238}U$ vs. $^{235}U/^{238}U$, a linear fit has $R^2 = 0.997$ and a slope of 0.004876 ± 0.000025 (2σ) and a y-intercept passing through the origin.

[Table 3]

While the samples display a large range of $^{235}U/^{238}U$ ratios, sample U1A and U1B are relatively homogeneous with respect to both chemical composition (see Table 1 and Figure 3) and uranium isotope ratios, except for the $^{235}U/^{238}U$ ratio of 11.8 measured near the periphery of U1B (Figures 8 and 9). The three measurements on U1A have a mean $^{235}U/^{238}U$ ratio of 3.5 and relative standard deviation of 9%. For U1B, the mean value of the $^{235}U/^{238}U$ ratios (excluding the 11.8 value) is 7.2, with a relative standard deviation of 8.2%. We found no systematic variation in the $^{235}U/^{238}U$ ratio with position in these two samples and our observations suggest U1A and U1B are relatively well mixed in both major elements and uranium isotopes.

Sample U1B exhibits a singularly high $^{235}U/^{238}U$ ratio near the periphery. We explored the spatial extent of this region by translating the stage ~20 μm and performing another U-isotope analysis. The $^{235}U/^{238}U$ ratio in this second location is 8.16 and is indistinguishable from values elsewhere in the sample, i.e.,

lower by a factor of ~1.5, suggesting U-isotope heterogeneity in sample U1B has a characteristic spatial scale of ~10 μm or less.

U3 exhibits much greater compositional (particularly with respect to Ca; Table 1 and Figure 3) or U isotope homogeneity compared to U1A or U1B (Figure 10). The relative standard deviations of the Ca concentration and $^{235}U/^{238}U$ ratios for U3 are 20% and 43%, respectively (compared with U1A's respective relative standard deviations of 7.5% and 9%). The large relative standard deviation in the $^{235}U/^{238}U$ ratio in U3 is due to several low values near the center of the sample. There are no features in the backscattered electron image or composition maps with which these low ratios are correlated, but autoradiography shows a low activity region near the center of the sample (Figure 3).

3.3 Correlations between uranium isotope ratios and major element composition

Samples U2 and U4 display correlations between the $^{235}U/^{238}U$ ratios and composition, specifically with the bright and dark regions visible in their respective backscattered electron images and compositional maps (Figures 3, 4, 11, 12; Table 2). In U2, two distinct U-isotope regions can be defined. One region, characterized by $1 < {}^{235}U/^{238}U < 8$, is associated with the brighter regions in the backscattered electron image and is enriched in CaO, Fe_2O_3, and MgO (Figures 3, 4), while the second region, characterized by $0.02 < {}^{235}U/^{238}U < 1$, is associated with the darker regions and is enriched in K_2O. The $^{235}U/^{238}U$ ratios in U4 also display a bimodal behavior, but exhibit just the opposite correlation between the $^{235}U/^{238}U$ ratio and brightness in the backscattered electron images (mean atomic number). The darker regions (enriched in SiO_2) in U4 are associated with higher $^{235}U/^{238}U$ ratios, $4 < {}^{235}U/^{238}U < 6.5$, while the brighter regions (enriched in CaO and Al_2O_3) correspond to $2 < {}^{235}U/^{238}U < 4$.

In two of the samples, U3 and U4, both the $^{235}U/^{238}U$ ratio and the uranium concentration was determined (Figure 13; Appendix A). The uranium concentrations range from 4 to 22 μg/g with an uncertainty of ~20% (this uncertainty is dominated by a 10% assumed on uncertainty for the $(^{235}U^{16}O^{+}+^{238}U^{16}O^{+})/^{30}Si^{+}$ ratio on both the sample and the standard), while the concentration of uranium in soil near ground zero ranges from 2.7 to 4.8 μg/g (Eppich et al., 2014).

[Figure 1]

[Figure 6]

[Figure 7]

[Figure 8]

[Figure 9]

[Figure 10]

[Figure 11]

[Figure 12]

[Figure 13]

4. Discussion

4.1 Compositional heterogeneity and fallout formation processes

U1A and U1B are quasi-homogeneous and may have been held above the melting temperature (~1300 K, determined by MELTS calculations of liquidus temperatures for glasses of these compositions; Ghiorso

and Sack, 1995; Asimow and Ghiorso, 1998) long enough or experienced a high enough temperature for the combined effects of convection and diffusion to effectively homogenize the melts. The compositional variation observed in U2 suggests this sample formed through the collision and mixing of two or more relatively large, molten objects of dissimilar composition. U3 exhibits compositional heterogeneity (primarily in Si and Ca) on a spatial scale of tens of microns, and the sharply delineated outlines of some of the high Si regions suggest that these regions may be inclusions of partially melted but incompletely homogenized quartz. U4 has many circular and elliptical regions of ~100 µm in size distributed along the periphery of the sample. These compositionally distinct regions suggest U4 may have also formed by the collision and agglomeration of a number of molten or partially molten objects of similar composition onto a large and homogenous molten droplet with a distinctly different composition, represented by the brighter region near the center of U4 (Figure 2).

4.2 Sequence of fallout formation inferred from uranium isotope heterogeneity

Given the correlation of the $^{235}U/^{238}U$ ratio with the major element composition in U2 and U4, we present a sequence of events that may have led to the formation of these glasses. Soil swept up into the fireball was melted and/or vaporized and interacted with device debris. Mixing between soil and unburned fuel created the observed enrichment in ^{235}U and the droplets then collided with other molten silicate droplets of different chemical and U-isotope compositions before cooling to form a solid spherule. The final agglomerated objects, U2 and U4, experienced mixing, but did not fully homogenize. The time scale for cooling of these objects was on the order of seconds (Glasstone, 1977; Izrael, 2002; Cassata et al., 2014).

4.3 Origin of uranium isotope heterogeneity

4.3.1 Mixing end members

The observed variation in U-isotope ratios in the spherules provides evidence for mixing between at least two components with different uranium isotopic compositions: one enriched in ^{235}U from the device, and the other reflecting natural isotopic composition uranium derived from soil and/or the device. In addition, U3 and U4 show reasonable positive correlations ($R^2 = 0.50$ and 0.73, respectively) between the $^{235}U/^{238}U$ ratio and the U concentration (Figure 3), implying higher concentrations of uranium represent a greater contribution of uranium enriched in ^{235}U from the device.

The maximum and minimum $^{235}U/^{238}U$ ratios are also consistent with two sources of uranium: highly enriched uranium (HEU) from the device and natural uranium from soil and/or the device. The maximum observed $^{235}U/^{238}U$ ratio, ~11.8 (~91.5% ^{235}U, assuming 1% ^{234}U) in sample U1B, approaches, but is still lower than, the $^{235}U/^{238}U$ ratio in oralloy ($^{235}U/^{238}U$~17.3, or ~93% enriched in ^{235}U), a type of highly enriched uranium common in the U.S. nuclear stockpile during the era of above ground testing (Moody, 1994). However, assuming the fuel was oralloy, measuring a $^{235}U/^{238}U$ of 17.3 in fallout would be surprising, due to mixing with natural uranium from soil and/or the device and neutron capture by ^{235}U during the detonation. The minimum measured $^{235}U/^{238}U$ ratio, ~0.02 in sample U2, approaches the $^{235}U/^{238}U$ value for uranium of natural isotopic composition, 0.00725.

The minor isotope ratios, $^{234}U/^{238}U$ and $^{236}U/^{238}U$, also illustrate mixing between two end members through their linear correlation on a uranium 3-isotope plot (Figures 6, 7), with all measurements having slopes and y-intercepts within uncertainties of each other.

4.3.2 Mixing between U-isotope components

Our observations allow us to calculate the relative contribution to each U-isotope measurement from the two, isotopically distinct end-members. Assuming (1) the only source of enriched uranium can be represented by oralloy from the device and (2) isotopic fractionation of uranium in the silicate melt can be neglected, we present a two-component mixing model demonstrating the uranium isotope compositions measured in the five fallout glasses can be explained by mixing enriched uranium from the device with natural uranium.

Let x_{234}, x_{235}, x_{236}, and x_{238} represent the abundances of ^{234}U, ^{235}U, ^{236}U, and ^{238}U in the enriched uranium end-member and y_{234}, y_{235}, and y_{238} the abundances of ^{234}U, ^{235}U and ^{238}U of uranium in the natural uranium end member. To a good approximation, ^{234}U makes up only ~0.0055% of the natural end member and can be neglected; ^{236}U has a vanishingly small abundance in natural uranium (Richter et al., 1999), and can also be neglected. With these assumptions, $y_{235} = 0.00725$ and $y_{238} = 0.9928$.
Conservation of mass requires

$$x_{234} + x_{235} + x_{236} + x_{238} = 1 \tag{1a}$$

and

$$y_{235} + y_{238} = 1. \tag{1b}$$

Let n_f and n_n represent, respectively, the contributions from the enriched and natural uranium end-members in an individual SIMS measurement. The number of atoms of each isotope in an individual measurement is given by:

$$^{234}U:\ n_{234} = n_f x_{234}, \tag{2a}$$

$$^{235}U:\ n_{235} = n_f x_{235} + n_n y_{235}, \tag{2b}$$

$$^{236}U:\ n_{236} = n_f x_{236}, \text{ and} \tag{2c}$$

$$^{238}U:\ n_{238} = n_f x_{238} + n_n y_{238}. \tag{2d}$$

The U-isotope ratios in fallout may then be represented as:

$$\frac{n_{234}}{n_{238}} = \frac{n_f x_{234}}{n_f x_{238} + n_n y_{238}}, \tag{3a}$$

$$\frac{n_{235}}{n_{238}} = \frac{n_f x_{235} + n_n y_{235}}{n_f x_{238} + n_n y_{238}}, \tag{3b}$$

$$\frac{n_{236}}{n_{238}} = \frac{n_f x_{236}}{n_f x_{238} + n_n y_{238}}, \text{ and} \tag{3c}$$

$$\frac{n_{236}}{n_{234}} = \frac{x_{236}}{x_{234}}. \tag{3d}$$

Equations 3a – 3d can be solved to determine the relative contributions from the two uranium isotope end-members to each isotope ratio measured in the SIMS analyses.

Solving equations 3a – 3d for n_n/n_f, the ratio of the number of uranium atoms in the natural end-member to the number of atoms from the enriched end-member, yields:

$$\frac{n_n}{n_f} = \frac{\frac{n_{238}}{n_{234}} x_{234} - x_{238}}{y_{238}}, \tag{4a}$$

$$\frac{n_n}{n_f} = \frac{x_{235} - \frac{n_{235}}{n_{238}} x_{238}}{\frac{n_{235}}{n_{238}} y_{238} - y_{235}}, \quad \text{and} \tag{4b}$$

$$\frac{n_n}{n_f} = \frac{\frac{n_{238}}{n_{236}} x_{236} - x_{238}}{y_{238}}. \tag{4c}$$

One solution to Equations 4a-4c is shown in Figure 14, where we use our data in combination with Equation 4b to illustrate the full range of mixing between uranium isotope end members. Similar diagrams can be constructed for equations 4a and 4c for ^{234}U and ^{236}U.

[Figure 14]

5. Conclusions

Five aerodynamic fallout glasses were analyzed using SIMS, SEM/EDS, EPMA, and autoradiography. Individual spherules display distinct compositional heterogeneity suggestive of rapid cooling and exhibit striking heterogeneity in U isotopes with $0.02 < {}^{235}U/{}^{238}U < 11.8$ among the five samples and $0.02 < {}^{235}U/{}^{238}U < 7.8$ within a single sample. The large heterogeneity in the uranium isotope ratios confirms that these aerodynamic fallout samples preserve a mixture of uranium from at least two end members with distinct uranium isotope compositions. The extent of mixing and the magnitude of uranium isotopic heterogeneity provide important constraints on the thermal history of aerodynamic fallout glasses, and point the way to developing a more quantitative understanding of the formation of fallout.

Two samples (U1A and U1B) are far more relatively homogenous with respect to both major element composition and uranium isotopes than the other three (U2, U3, and U4), suggesting these objects had longer residence times within the fireball at high temperature or were formed from approximately homogenous precursors, with respect to composition and uranium isotopics. The $^{235}U/^{238}U$ ratio is correlated with major element composition in two samples, suggesting agglomeration of molten or partially molten precursors tens to hundreds of microns in size, followed by rapid cooling. Correlated variations among the ^{234}U, ^{235}U, ^{236}U and ^{238}U abundances point to mixing between end-member components corresponding to highly enriched uranium derived from the device and natural uranium. We developed a two-component mixing model, one end member being natural uranium and the other having the composition of oralloy (HEU), to illustrate the range of mixing in the aerodynamic fallout glasses. Our measurements suggest that residual fuel was distributed throughout the volumes of all of the samples prior to solidification. Future experiments will examine the variations in uranium isotope compositions among aerodynamic fallout samples spanning a broader range of sizes and distance of collection from ground zero.

Acknowledgments

We thank Christina Ramon for help with sample preparation, Ross Williams and Kerri Schorzman for ICP-MS measurements, Gary Eppich, Ben Jacobsen, and Naomi Marks for helpful discussions, and Gary Stone and Anna Lindquist for performing the autoradiography. This research was performed under appointment to the Nuclear Nonproliferation International Safeguards Graduate Fellowship Program sponsored by the National Nuclear Security Administration's (NNSA's) Next Generation Safeguards Initiative (NGSI). This work was supported by the Laboratory Directed Research and Development Program (project 10-SI-016) at LLNL and the NNSA Office of Defense Nuclear Nonproliferation Research and Development and performed under the auspices of the U.S. Department of Energy by Lawrence Livermore National Laboratory under Contract DE-AC52-07NA27344.

References

Adams, C. E., & O'Connor, J. D. (1957). *The nature of individual radioactive particles VI. Fallout particles from a tower shot, Operation Redwing*. No. USNRDL-TR-208. U.S. Naval Radiological Defense Lab., San Francisco, CA (United States).

Adams, C. E., Farlow, N. H., & Schell, W. R. (1960). The compositions, structures and origins of radioactive fall-out particles. *Geochimica et Cosmochimica Acta*, *18*(1), 42-56.

Asimow, P. D., & Ghiorso, M. S. (1998). Algorithmic modifications extending MELTS to calculate subsolidus phase relations. *American Mineralogist*, *83*, 1127-1132.

Armstrong, J. T. (1995). CITZAF – A package of correction programs for the quantitiative electron microbeam x-ray analysis of thick polished materials, thin films, and particles. *Microbream Analysis, 4(3), 177-200.*

Crocker, G. R., O'Connor, J. D., & Freiling, E. C. (1965). *Physical and radiochemical properties of fallout particles*. No. USNRDL-TR-899. U.S. Naval Radiological Defense Lab., San Francisco, CA (United States).

Belloni, F., Himbert, J., Marzocchi, O., & Romanello, V. (2011). Investigating incorporation and distribution of radionuclides in trinitite. *Journal of environmental radioactivity*, *102*(9), 852-862.

Bellucci, J. J., & Simonetti, A. (2012). Nuclear forensics: searching for nuclear device debris in trinitite-hosted inclusions. *Journal of Radioanalytical and Nuclear Chemistry*, *293*(1), 313-319.

Bellucci, J. J., Simonetti, A., Wallace, C., Koeman, E. C., & Burns, P. C. (2013). Isotopic fingerprinting of the world's first nuclear device using post-detonation materials. *Analytical Chemistry*, *85*(8), 4195-4198.

Bellucci, J. J., Simonetti, A., Koeman, E. C., Wallace, C., & Burns, P. C. (2014). A detailed geochemical investigation of post-nuclear detonation trinitite glass at high spatial resolution: Delineating anthropogenic vs. natural components. *Chemical Geology*, *365*, 69-86.

Brode, H. L. (1968). Review of nuclear weapons effects. *Annual Review of Nuclear Science*, *18*(1), 153-202.

Cassata, W. S., Prussin, S. G., Knight, K. B., Hutcheon, I. D., Isselhardt, B. H., & Renne, P. R. (2014). When the dust settles: stable xenon isotope constraints on the formation of nuclear fallout. *Journal of Environmental Radioactivity*, *137*, 88-95.

Eby, N., Hermes, R., Charnley, N., & Smoliga, J. A. (2010). Trinitite—the atomic rock. *Geology Today*, *26*(5), 180-185.

Eppich, G. R., Knight, K. B., Jacomb-Hood, T. W., Spriggs, G. D., & Hutcheon, I. D. (2014). Constraints on fallout melt glass formation from a near-surface nuclear test. *Journal of Radioanalytical and Nuclear Chemistry*, 1-17.

Fahey, A. J., Zeissler, C. J., Newbury, D. E., Davis, J., & Lindstrom, R. M. (2010). Post-detonation nuclear debris for attribution. *Proceedings of the National Academy of Sciences*, *107*(47), 20207-20212.

Glasstone, S., & Dolan, P. J. (1977). *The Effects of Nuclear Weapons*. US Department of Defense &US Department of Energy.

Ghiorso, M. S., & Sack, R. O. (1995). Chemical mass transfer in magmatic processes IV. A revised and internally consistent thermodynamic model for the interpolation and extrapolation of liquid-solid equilibria in magmatic systems at elevated temperatures and pressures. *Contributions to Mineralogy and Petrology*, *119* (2-3), 197-212.

Gostic, R. C., Knight, K. B., Spriggs, G., & Hutcheon, I. D. (2012). Taking a second look: Re-examining ground collected fallout from low yield surface nuclear tests for forensic signatures. Paper presented at the Methods & Applications of Radioanalytical Chemistry conference in Kailua-Kona, HI, USA.

Izrael, Y. A. (2002). *Radioactive Fallout after Nuclear Explosions and Accidents*. Elsevier.

Miller, C. F. (1964). *Biological and radiological effects of fallout from nuclear explosions.* No. IMU-4536. Stanford Research Institute, Menlo Park, CA (United States).

Moody, K. J. (1994). *Dissolved oralloy standards and the origin of HEU*. No. UCRL-ID-117611. Lawrence Livermore National Lab., Livermore, CA (United States).

Parekh, P. P., Semkow, T. M., Torres, M. A., Haines, D. K., Cooper, J. M., Rosenberg, P. M., & Kitto, M. E. (2006). Radioactivity in trinitite six decades later. *Journal of Environmental Radioactivity*, *85*(1), 103-120.

Tompkins, R. C., Russell, I. J., & Nathans, M. W. (1970). *Comparison between cloud samples and close-in ground fallout samples from nuclear ground bursts.* Army Ballistic Research Lab., Aberdeen Proving Ground, Md (United States).

Wallace, C., Bellucci, J. J., Simonetti, A., Hainley, T., Koeman, E. C., & Burns, P. C. (2013). A multi-method approach for determination of radionuclide distribution in trinitite. *Journal of Radioanalytical and Nuclear Chemistry*, *298*(2), 993-1003.

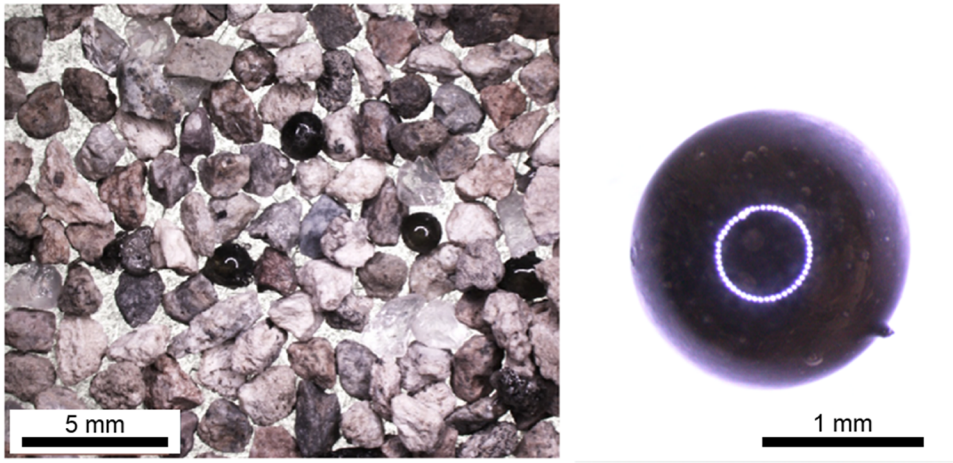

Figure 1: Optical images of size-sorted fallout (left) showing distinct dark glassy aerodynamic shapes mixed with soil fragments, and (right) and an isolated piece of aerodynamic fallout glass. The bright artifact in the center of the isolated aerodynamic fallout glass is the ring light from the optical microscope, which also highlights the high degree of symmetry in these objects.

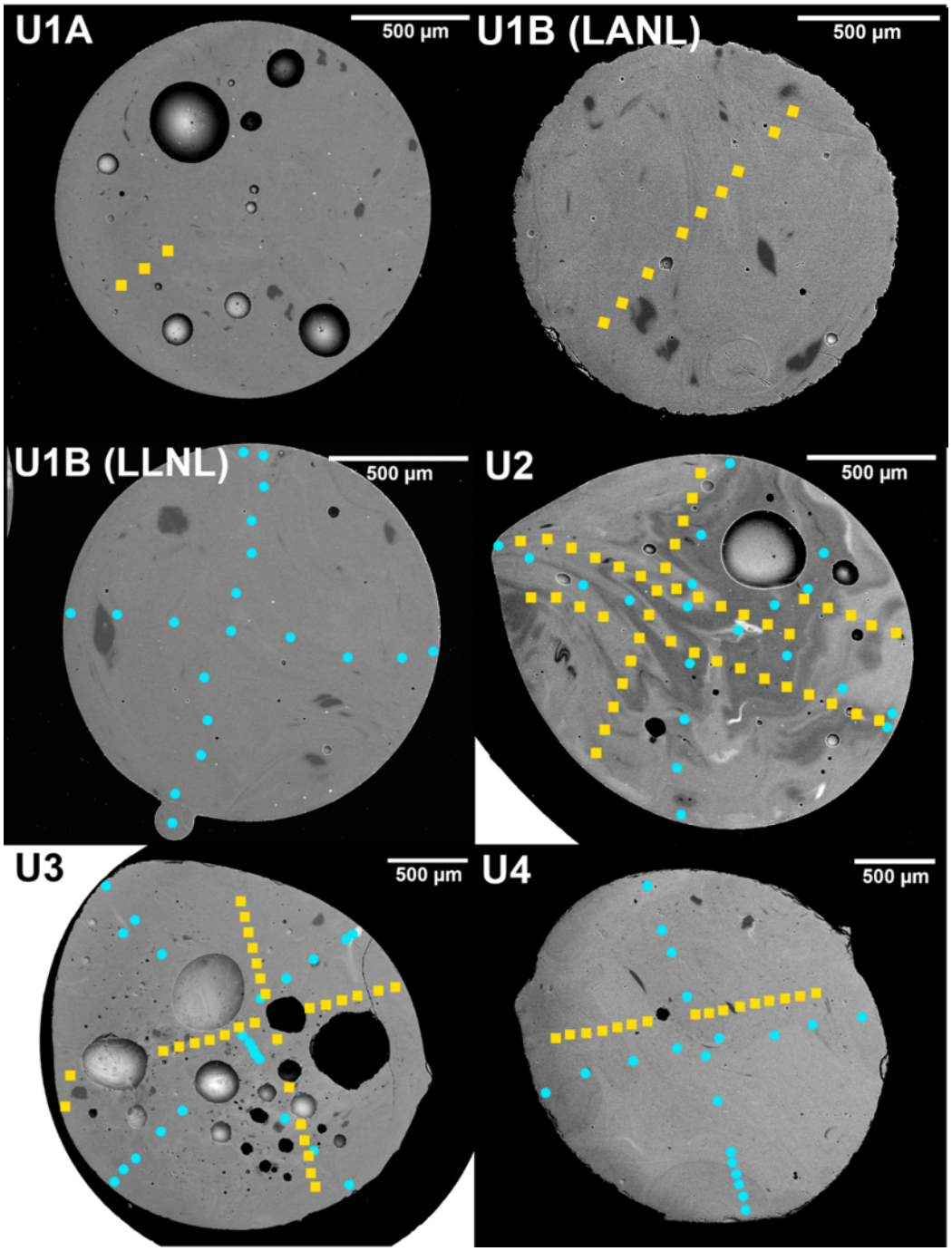

Figure 2: Backscattered electron images of fallout glasses analyzed by SIMS (images taken prior to SIMS analyses) overlaid with the SIMS analysis locations. The contrast of each image was individually adjusted to emphasize compositional zoning features and no inferences about compositional differences between the samples should be drawn from these images. Filled blue circles show the locations of the LLNL SIMS analyses (spot size: ~10-20 µm), while filled yellow squares show the locations of the LANL SIMS analyses (raster size: 25 x 25 µm). The markers have been enlarged to ease viewing and are not representative of the actual size of the SIMS analyses. Sample U1B is shown twice, as this sample was initially analyzed at LLNL, then repolished to expose a different surface, and subsequently analyzed at LANL.

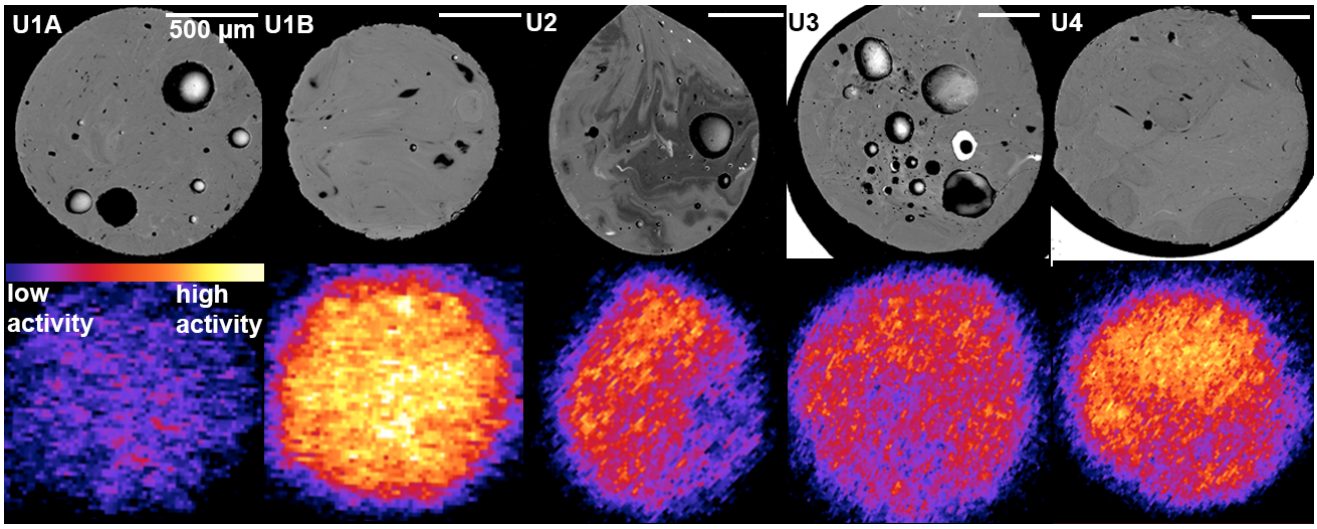

Figure 3: Backscattered electron (top) and autoradiography (bottom) images of the fallout glasses characterized in this study. Backscattered electron micrographs show polished mid-sections of the samples; brightness reflects average atomic number, with brighter areas having a higher average atomic number. The contrast of each image was individually adjusted to emphasize compositional zoning features and no inferences about compositional differences between the samples should be drawn from these images. The bright region towards the center of sample U3 is sample charging. On the bottom, false color qualitative autoradiography images indicate both α and β activity (but is likely dominated by β activity due to the low specific activity of uranium in these samples), where yellow-white areas depict areas of highest activity. All five images were obtained from the same exposure and differences in color reflect relative differences in activity. Scale bars are all 500 µm.

Table 1: Average major element compositions in wt.% determined by EPMA

	# pts	SiO_2	1σ*	Al_2O_3	1σ*	CaO	1σ*	K_2O	1σ*	Na_2O	1σ*	Fe_2O_3	1σ*	TiO_2	1σ*	MnO	1σ*	MgO	1σ*	Sum
U1A	39	72.36	1.35	14.56	0.81	1.41	0.18	3.69	0.12	3.11	0.15	3.67	0.22	0.33	0.02	0.13	0.02	0.60	0.06	99.86
U1B	49	71.75	0.74	14.49	0.52	1.84	0.14	3.64	0.11	3.12	0.10	3.44	0.21	0.28	0.03	0.09	0.02	0.58	0.04	99.23
U2	48	72.18	1.99	13.49	1.25	1.10	0.61	4.94	0.53	3.72	0.41	2.27	0.83	0.23	0.06	0.11	0.03	0.38	0.20	98.42
U3	44	71.43	1.67	13.65	1.02	2.55	0.51	3.87	0.21	3.36	0.22	3.27	0.21	0.29	0.03	0.15	0.02	0.64	0.06	99.21
U4	49	71.90	4.08	14.30	2.27	2.61	0.76	3.54	0.54	2.97	0.46	3.22	0.50	0.29	0.05	0.13	0.03	0.56	0.10	99.52

* One standard deviation of multiple analyses

Table 2: Average major element compositions in wt.% determined by EPMA for samples U2 and U4 separated into measurements made in the bright and dark regions, as determined from the backscattered electron image

	# pts	SiO_2	1σ*	Al_2O_3	1σ*	CaO	1σ*	K_2O	1σ*	Fe_2O_3	1σ*	MgO	1σ*
U2 (bright)	14	70.93	1.38	13.34	1.20	1.79	0.19	4.44	0.21	3.20	0.27	0.59	0.07
U2 (dark)	13	72.83	0.92	14.06	0.61	0.45	0.24	5.50	0.29	1.36	0.22	0.16	0.07
U4 (bright)	13	69.59	0.59	15.54	0.40	3.37	0.14	3.44	0.06	3.18	0.10	0.58	0.02
U4 (dark)	17	72.51	1.02	13.96	0.56	2.14	0.39	3.71	0.28	3.37	0.26	0.58	0.06

* One standard deviation of multiple analyses

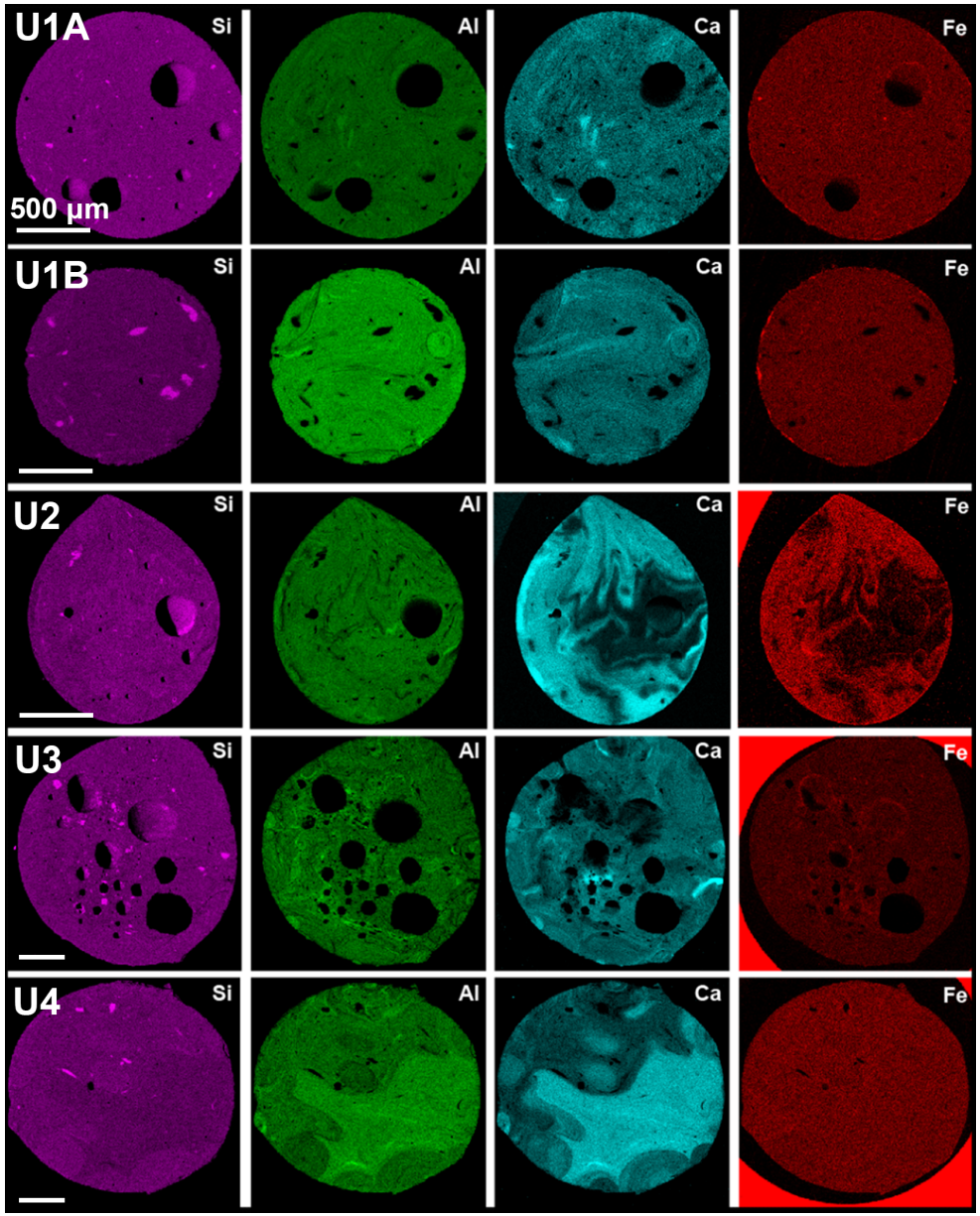

Figure 4: Chemical composition maps of Si, Al, Ca, and Fe (respectively) determined from wavelength-dispersive x-ray spectrometry mapping using EPMA. All

scale bars are 500 µm.

Table 3: SIMS measurements of $^{235}U/^{238}U$ in aerodynamic fallout glasses

U1A	$^{235}U/^{238}U$	2σ	$^{234}U/^{238}U$	2σ	$^{236}U/^{238}U$	2σ
LANL-1	3.85	0.06	0.042	0.00179365	0.018	0.001105913
LANL-2	3.08	0.05	0.033	0.001693282	0.015	0.001104707
LANL-3	3.52	0.07	0.038	0.002886993	0.019	0.001505636

U1B	$^{235}U/^{238}U$	2σ	$^{234}U/^{238}U$	2σ	$^{236}U/^{238}U$	2σ
LANL - 1	7.61	0.10	0.084	0.0025	0.036	0.0017
LANL - 2	7.34	0.09	0.079	0.0023	0.035	0.0014
LANL - 3	6.14	0.08	0.067	0.0021	0.030	0.0013
LANL - 4	7.17	0.09	0.077	0.0025	0.034	0.0014
LANL - 5	7.26	0.09	0.078	0.0023	0.036	0.0015
LANL - 6	8.64	0.12	0.094	0.0029	0.042	0.0017
LANL - 7	7.12	0.10	0.076	0.0023	0.036	0.0015
LANL - 8	6.28	0.09	0.066	0.0028	0.030	0.0014
LANL - 9	7.05	0.24	0.079	0.0063	0.033	0.0032
LANL - 10	7.25	0.10	0.078	0.0029	0.035	0.0016
LANL - 11	7.45	0.10	0.080	0.0027	0.036	0.0015
LANL - 12	6.08	0.11	0.065	0.0027	0.029	0.0015
LLNL - 1	6.57	0.13				
LLNL - 2	7.21	0.15				
LLNL - 3	7.18	0.17				
LLNL - 4	7.96	0.12				
LLNL - 5	7.42	0.14				
LLNL - 6	7.32	0.11				
LLNL - 7	7.08	0.1				
LLNL - 8	7.72	0.11				
LLNL - 9	8.02	0.11				
LLNL - 10	6.67	0.09				
LLNL - 11	6.77	0.10				
LLNL - 12	6.86	0.09				
LLNL - 13	6.35	0.05				
LLNL - 14	7.07	0.13				
LLNL - 15	6.77	0.15				
LLNL - 16	6.57	0.12				
LLNL - 17	7.06	0.15				
LLNL - 18	11.84	0.22				
LLNL - 19	8.16	0.13				

U2	$^{235}U/^{238}U$	2σ	$^{234}U/^{238}U$	2σ	$^{236}U/^{238}U$	2σ
LANL-1	3.37	0.04	0.0360	0.0016	0.0175	0.0010
LANL-2	3.84	0.05	0.0416	0.0014	0.0197	0.0009
LANL-3	2.18	0.08	0.0239	0.0011	0.0113	0.0006
LANL-4	1.22	0.01	0.0131	0.0005	0.0061	0.0003
LANL-5	3.19	0.03	0.0346	0.0009	0.0164	0.0007
LANL-6	3.09	0.02	0.0336	0.0008	0.0156	0.0006
LANL-7	1.58	0.02	0.0174	0.0006	0.0079	0.0004
LANL-8	2.60	0.08	0.0282	0.0012	0.0131	0.0005
LANL-9	2.95	0.03	0.0318	0.0008	0.0150	0.0005
LANL-10	0.61	0.01	0.0071	0.0003	0.0031	0.0003
LANL-11	0.84	0.03	0.0095	0.0005	0.0044	0.0003
LANL-12	2.34	0.04	0.0256	0.0008	0.0119	0.0006
LANL-13	5.72	0.05	0.0625	0.0012	0.0280	0.0008
LANL-14	2.63	0.03	0.0289	0.0009	0.0130	0.0007
LANL-15	4.60	0.04	0.0488	0.0011	0.0223	0.0007
LANL - 16	5.01	0.05	0.0544	0.0013	0.0246	0.0007
LANL - 17	4.30	0.04	0.0468	0.0012	0.0211	0.0008
LANL - 18	0.04	0.00	0.0005	0.0001	0.0002	0.0001
LANL - 19	2.77	0.03	0.0297	0.0007	0.0133	0.0004
LANL - 20	0.08	0.00	0.0008	0.0002	0.0004	0.0001
LANL - 21	0.11	0.00	0.0013	0.0001	0.0006	0.0001
LANL - 22	0.17	0.00	0.0017	0.0002	0.0008	0.0001
LANL - 23	1.23	0.01	0.0129	0.0005	0.0062	0.0004
LANL - 24	3.89	0.04	0.0427	0.0012	0.0193	0.0008
LANL - 25	0.75	0.01	0.0078	0.0004	0.0036	0.0003
LANL - 26	1.16	0.02	0.0126	0.0006	0.0055	0.0004
LANL - 27	4.45	0.04	0.0479	0.0011	0.0212	0.0008
LANL - 28	3.01	0.02	0.0328	0.0008	0.0146	0.0007
LANL - 29	3.34	0.03	0.0360	0.0009	0.0165	0.0006
LANL - 30	0.192	0.003	0.0020	0.0002	0.0010	0.0001
LANL - 31	0.301	0.005	0.0033	0.0003	0.0016	0.0002
LANL - 32	0.052	0.002	0.0005	0.0001	0.0002	0.0001
LANL - 33	0.034	0.002	0.0003	0.0001	0.0002	4.85E-05
LANL - 34	0.126	0.002	0.0013	0.0001	0.0006	0.0001
LANL - 35	0.288	0.004	0.0029	0.0002	0.0015	0.0001

U2 (cont.)	$^{235}U/^{238}U$	2σ	$^{234}U/^{238}U$	2σ	$^{236}U/^{238}U$	2σ
LANL-36	5.13	0.04	0.0553	0.0012	0.0248	0.0008
LANL-37	1.04	0.03	0.0110	0.0004	0.0048	0.0003
LANL-38	2.34	0.02	0.0256	0.0007	0.0111	0.0004
LANL-39	2.39	0.04	0.0253	0.0008	0.0117	0.0005
LANL-40	4.47	0.05	0.0476	0.0010	0.0215	0.0007
LANL-41	5.13	0.04	0.0546	0.0011	0.0239	0.0007
LANL-42	5.23	0.04	0.0566	0.0013	0.0250	0.0008
LANL-43	4.96	0.04	0.0532	0.0010	0.0235	0.0006
LANL-44	5.97	0.06	0.0647	0.0016	0.0288	0.0011
LANL-45	5.42	0.05	0.0586	0.0015	0.0261	0.0011
LLNL-1	7.41	0.24				
LLNL-2	3.76	0.15				
LLNL-3	2.85	0.10				
LLNL-4	2.83	0.12				
LLNL-5	4.13	0.18				
LLNL-6	1.47	0.09				
LLNL-7	0.11	0.01				
LLNL-8	4.71	0.14				
LLNL-9	3.74	0.15				
LLNL-10	2.12	0.03				
LLNL-11	4.69	0.18				
LLNL-12	5.01	0.14				
LLNL-13	2.71	0.13				
LLNL-14	0.020	0.002				
LLNL-15	2.81	0.10				
LLNL-16	0.20	0.01				
LLNL-17	1.01	0.04				
LLNL-18	0.23	0.01				
LLNL-19	0.32	0.02				
LLNL-20	0.35	0.01				

Table 3 (continued): SIMS measurements of $^{235}U/^{238}U$ in aerodynamic fallout glasses

U3	$^{235}U/^{238}U$	2σ	$^{234}U/^{238}U$	2σ	$^{236}U/^{238}U$	2σ
LANL - 1	3.24	0.08	0.0343	0.0023	0.0158	0.0015
LANL - 2	2.18	0.03	0.0242	0.0012	0.0110	0.0008
LANL - 3	3.12	0.04	0.0337	0.0012	0.0144	0.0008
LANL - 4	3.77	0.05	0.0403	0.0013	0.0177	0.0009
LANL - 5	3.84	0.04	0.0423	0.0014	0.0181	0.0010
LANL - 6	3.90	0.05	0.0425	0.0015	0.0196	0.0009
LANL - 7	3.66	0.03	0.0401	0.0009	0.0178	0.0006
LANL - 8	1.13	0.01	0.0127	0.0006	0.0055	0.0004
LANL - 9	2.05	0.02	0.0221	0.0007	0.0100	0.0005
LANL - 10	2.92	0.03	0.0316	0.0008	0.0141	0.0005
LANL - 11	4.03	0.04	0.0430	0.0010	0.0197	0.0007
LANL - 12	3.78	0.04	0.0399	0.0012	0.0179	0.0008
LANL - 13	4.58	0.04	0.0495	0.0013	0.0231	0.0009
LANL - 14	5.71	0.07	0.0613	0.0021	0.0285	0.0012
LANL - 15	4.71	0.06	0.0501	0.0016	0.0229	0.0010
LANL - 16	3.83	0.04	0.0413	0.0016	0.0185	0.0008
LANL - 17	2.52	0.03	0.0271	0.0009	0.0127	0.0006
LANL - 18	3.21	0.03	0.0344	0.0011	0.0153	0.0007
LANL - 19	4.63	0.05	0.0506	0.0015	0.0231	0.0009
LANL - 20	4.52	0.05	0.0483	0.0014	0.0223	0.0009
LANL - 21	1.10	0.02	0.0118	0.0006	0.0054	0.0004
LANL - 22	0.52	0.01	0.0055	0.0004	0.0025	0.0003
LANL - 23	4.12	0.04	0.0442	0.0013	0.0202	0.0009
LANL - 24	4.03	0.04	0.0434	0.0013	0.0196	0.0008
LANL - 25	5.32	0.05	0.0576	0.0015	0.0260	0.0009
LANL - 26	6.57	0.06	0.0708	0.0014	0.0321	0.0010
LANL - 27	4.41	0.05	0.0477	0.0013	0.0218	0.0009
LANL - 28	5.15	0.05	0.0572	0.0014	0.0247	0.0009
LLNL - 1	5.45	0.11				
LLNL - 2	4.39	0.12				
LLNL - 3	5.48	0.11				
LLNL - 4	4.28	0.10				
LLNL - 5	3.97	0.11				
LLNL - 6	1.91	0.08				
LLNL - 7	3.16	0.09				
LLNL - 8	4.09	0.10				
LLNL - 9	4.32	0.10				
LLNL - 10	6.78	0.18				
LLNL - 11	4.90	0.11				
LLNL - 12	4.47	0.11				
LLNL - 13	6.11	0.19				
LLNL - 14	4.47	0.12				
LLNL - 15	3.08	0.06				

U3 (cont.)	$^{235}U/^{238}U$	2σ	$^{234}U/^{238}U$	2σ	$^{236}U/^{238}U$	2σ
LLNL - 16	0.41	0.03				
LLNL - 17	1.15	0.03				
LLNL - 18	0.24	0.01				
LLNL - 19	0.90	0.06				
LLNL - 20	2.63	0.08				
LLNL - 21	3.04	0.08				
LLNL - 22	4.32	0.14				

U4	$^{235}U/^{238}U$	2σ	$^{234}U/^{238}U$	2σ	$^{236}U/^{238}U$	2σ
LANL - 1	4.71	0.07	0.0491	0.0028	0.0230	0.0016
LANL - 2	4.60	0.07	0.0523	0.0024	0.0237	0.0016
LANL - 3	4.64	0.06	0.0496	0.0026	0.0235	0.0016
LANL - 4	3.94	0.07	0.0430	0.0024	0.0216	0.0016
LANL - 5	3.81	0.06	0.0416	0.0022	0.0180	0.0014
LANL - 6	3.08	0.04	0.0332	0.0017	0.0154	0.0012
LANL - 7	3.22	0.03	0.0344	0.0018	0.0157	0.0012
LANL - 8	3.95	0.05	0.0443	0.0022	0.0198	0.0015
LANL - 9	4.20	0.05	0.0461	0.0022	0.0204	0.0015
LANL - 10	3.87	0.05	0.0423	0.0024	0.0197	0.0015
LANL - 11	5.22	0.07	0.0565	0.0026	0.0255	0.0018
LANL - 12	4.74	0.07	0.0491	0.0024	0.0234	0.0017
LANL - 13	5.24	0.06	0.0588	0.0028	0.0243	0.0018
LANL - 14	5.15	0.07	0.0565	0.0030	0.0255	0.0018
LANL - 15	5.16	0.07	0.0557	0.0033	0.0243	0.0020
LANL - 16	5.34	0.07	0.0593	0.0032	0.0268	0.0020
LLNL - 1	5.89	0.14				
LLNL - 2	6.24	0.12				
LLNL - 3	5.71	0.11				
LLNL - 4	6.09	0.11				
LLNL - 5	1.90	0.05				
LLNL - 6	3.92	0.08				
LLNL - 7	2.96	0.06				
LLNL - 8	2.94	0.06				
LLNL - 9	4.32	0.12				
LLNL - 10	5.10	0.12				
LLNL - 11	5.43	0.12				
LLNL - 12	5.86	0.13				
LLNL - 13	5.16	0.14				
LLNL - 14	4.67	0.10				
LLNL - 15	3.05	0.08				
LLNL - 16	5.85	0.15				
LLNL - 17	2.46	0.07				
LLNL - 18	3.31	0.08				
LLNL - 19	2.11	0.05				

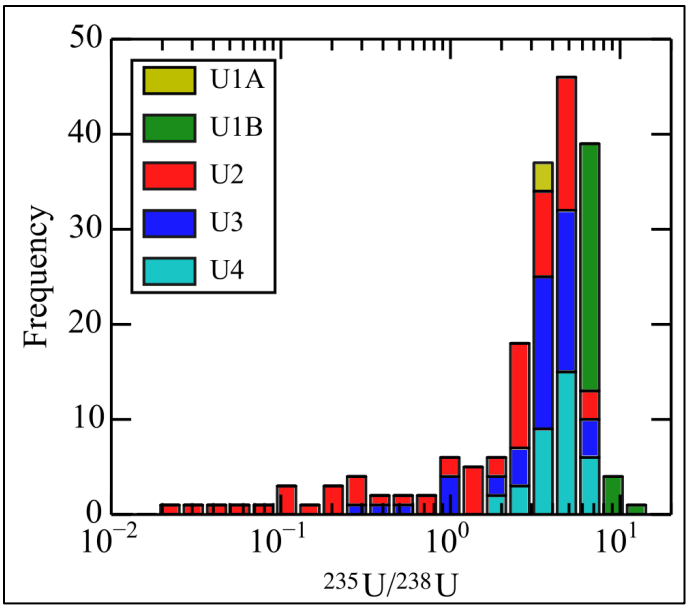

Figure 2: Histogram of the $^{235}U/^{238}U$ values in all five samples from both LLNL and LANL measurements. There are 25 bins spaced equally between $^{235}U/^{238}U$=0.01 and $^{235}U/^{238}U$=20. The preponderance of low $^{235}U/^{238}U$ ratios in U2, contrasted with higher values in U1B and U4 is apparent.

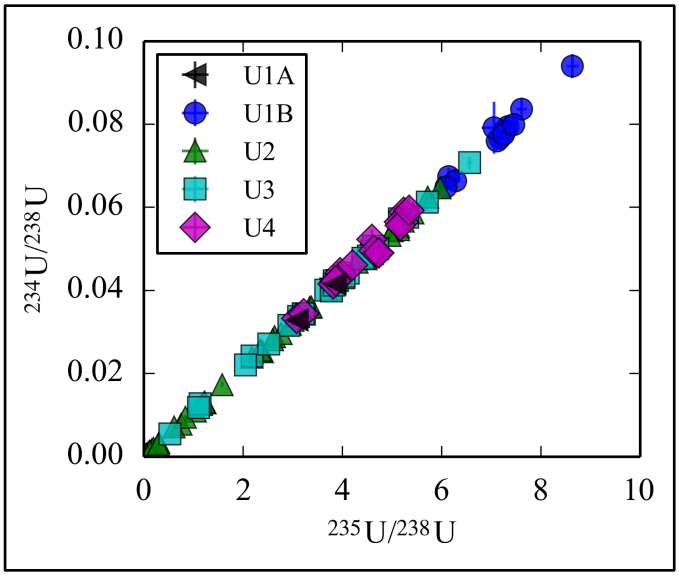

Figure 6: Composite 3-isotope correlation diagram for the 5 aerodynamic glasses showing $^{234}U/^{238}U$ vs. $^{235}U/^{238}U$; uncertainties are 2σ. Data are from LANL.

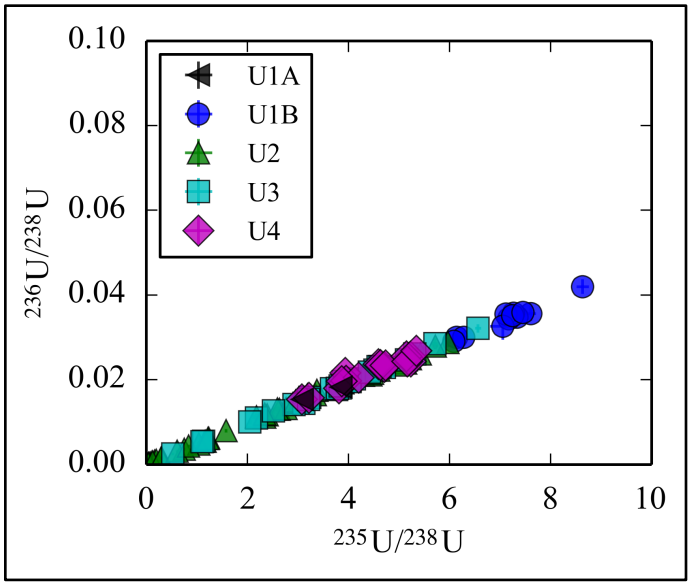

Figure 7: Composite 3-isotope correlation diagram for the 5 aerodynamic glasses showing $^{236}U/^{238}U$ vs. $^{235}U/^{238}U$; uncertainties are 2σ. Data are from LANL.

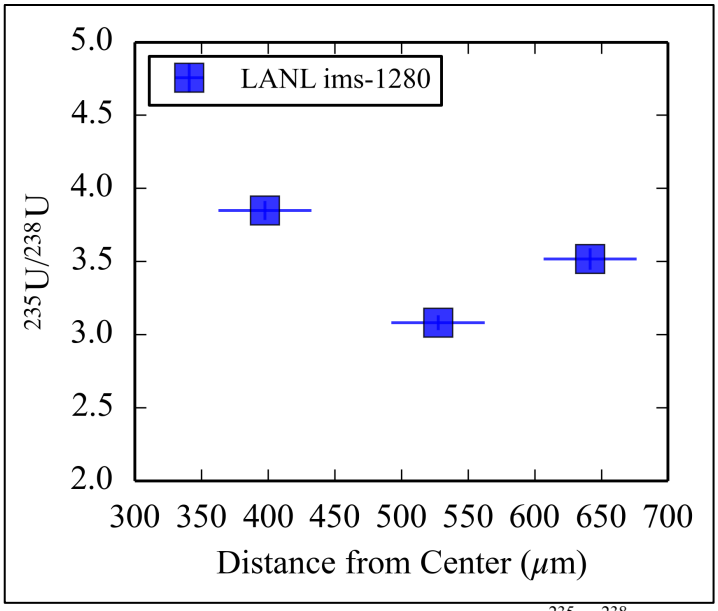

Figure 8: U isotope data for sample U1A showing the lack of variation in $^{235}U/^{238}U$ with distance from the center of the sample. Uncertainties are 2σ. Data are from LANL.

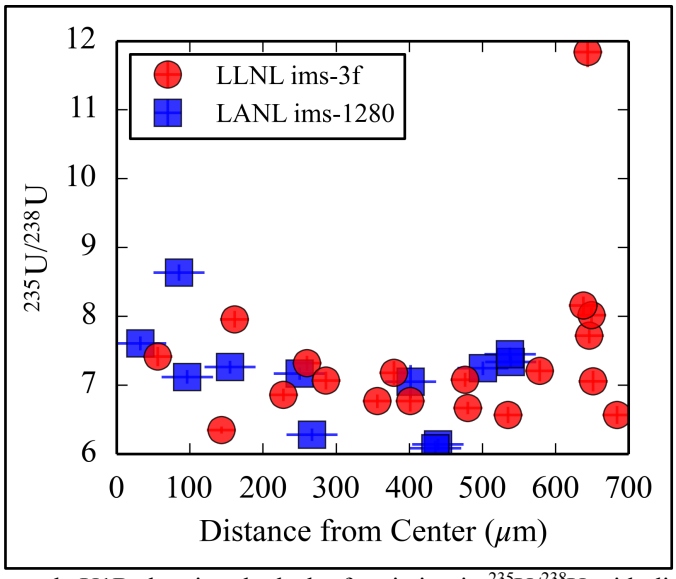

Figure 9: U isotope data for sample U1B showing the lack of variation in $^{235}U/^{238}U$ with distance from the center of the sample and the singularly high $^{235}U/^{238}U$ ratio of 11.8 near the periphery. Uncertainties are 2σ. Data are from LANL and LLNL.

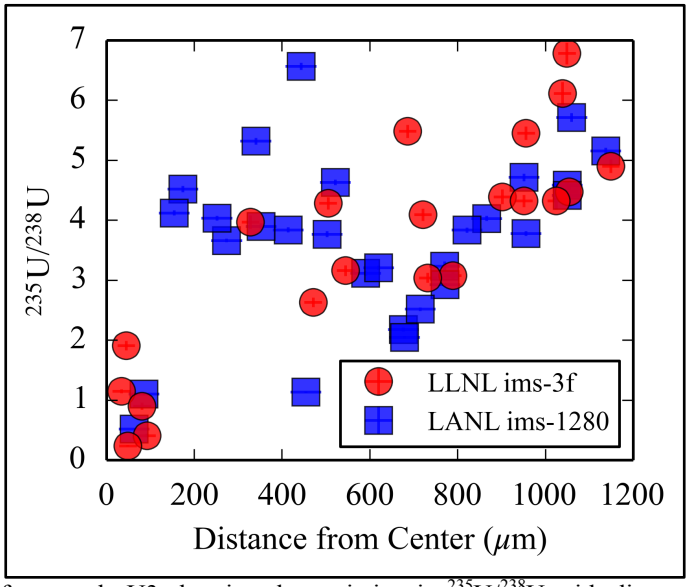

Figure 10: U isotope data for sample U3 showing the variation in $^{235}U/^{238}U$ with distance from the center of the sample. Uncertainties are 2σ. Data are from LANL and LLNL.

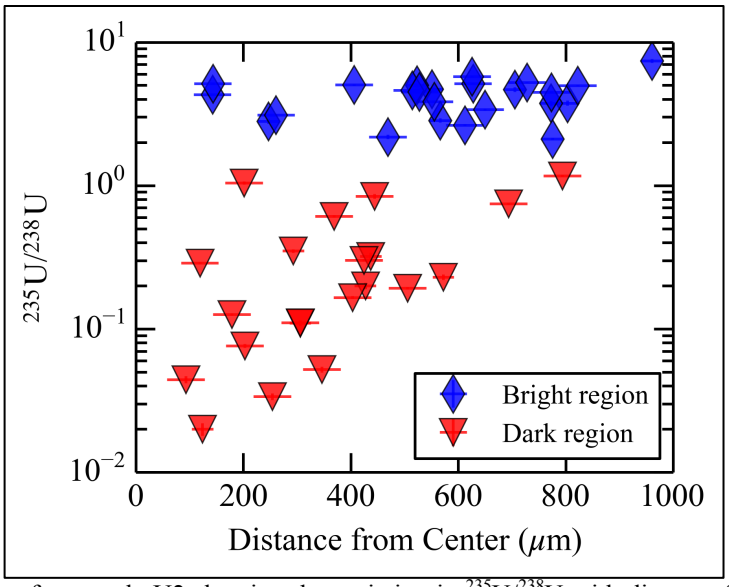

Figure 11: U isotope data for sample U2 showing the variation in $^{235}U/^{238}U$ with distance from the center; note the logarithmic ordinate scale. Uncertainties are 2σ. Data are from LANL and LLNL. Data are separated into SIMS measurements taken in the bright and dark regions, as defined in the text and shown in the backscattered electron image (Fig. 2).

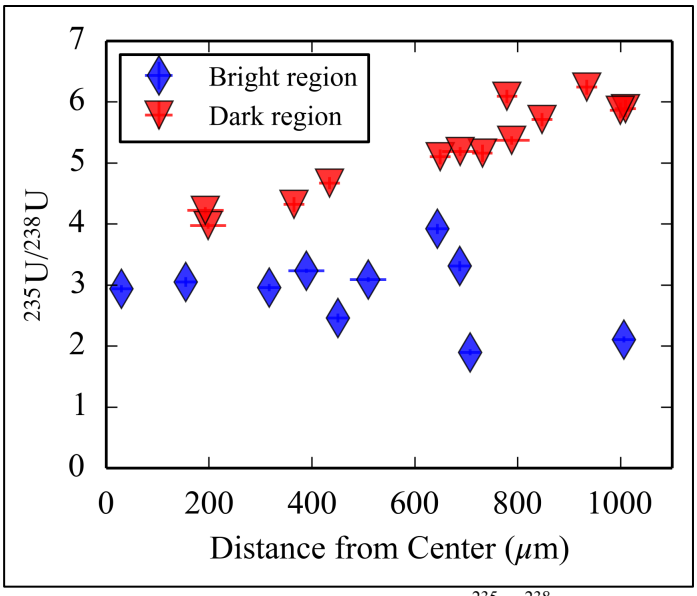

Figure 12: U isotope data for sample U4 showing the variation in the $^{235}U/^{238}U$ ratio with distance from the center. Uncertainties are 2σ. Data are from LANL and LLNL. Data are separated into SIMS measurements from the Ca-rich and Ca-poor regions, as defined in the text.

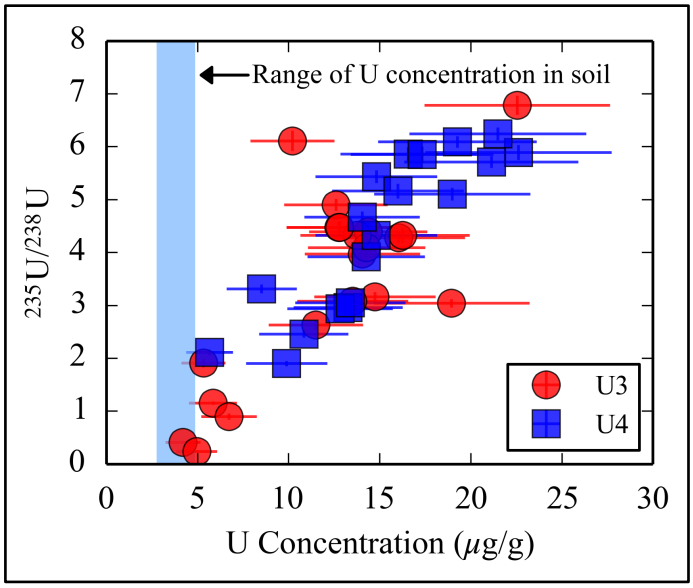

Figure 13: $^{235}U/^{238}U$ vs. uranium concentration for samples U3 and U4 showing the variation in the $^{235}U/^{238}U$ as a function of U concentration; uncertainties are 2σ. Data are from LLNL. The vertical bar represents the range of U concentrations measured in five soil samples proximate to ground zero (between 2.7 and 4.8 µg/g; Eppich et al., 2014).

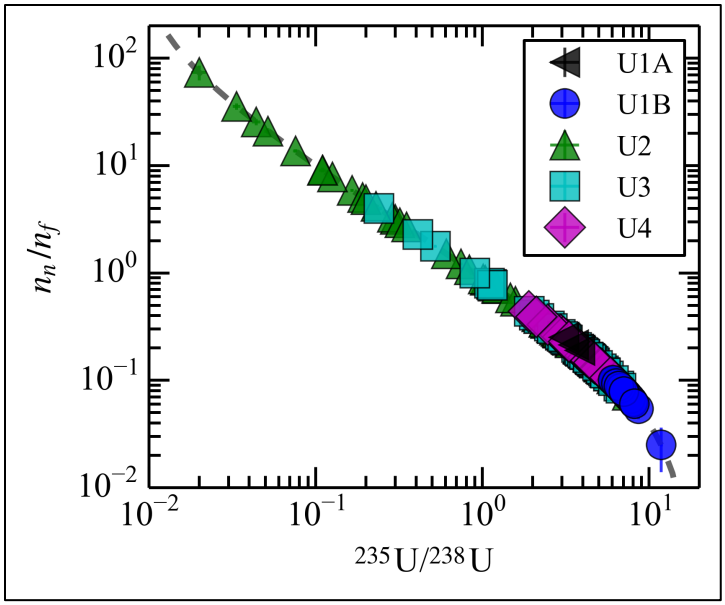

Figure 14: Contributions of uranium of natural isotopic composition (n_n) relative to uranium from the enriched (HEU) end-member (n_f) as a function of the $^{235}U/^{238}U$ ratio for samples U1A, U1B, U2, U3, and U4, calculated from Equation (4c). The dashed line represents the solution to Equation (4c) and depicts the shape of the mixing line. The mixing line asymptotically approaches infinity as the $^{235}U/^{238}U$ ratio approaches the composition of natural uranium, $^{235}U/^{238}U = 0.00725$, and asymptotically approaches zero as the $^{235}U/^{238}U$ ratio approaches 17.3, the $^{235}U/^{238}U$ ratio in oralloy (Moody, 1994). Most of the uncertainties (2σ) are smaller than the points.

Appendix A: U Concentration Data for Samples U3 and U4

Sample U3		**Sample U4**	
µg/g	**2σ**	**µg/g**	**2σ**
14	3	23	5
16	4	21	5
14	3	21	5
5	1	19	4
15	3	10	2
14	3	14	3
14	3	13	3
23	5	13	3
13	3	15	3
13	3	19	4
10	2	15	3
13	3	17	4
14	3	16	4
4	1	14	3
6	1	13	3
5	1	17	4
7	2	11	2
11	3	9	2
19	4	6	1
16	4		